Journal of the Korean Astronomical Society
50: 93 ∼ 103, 2017 August

https://doi.org/10.5303/JKAS.2017.50.4.93
pISSN: 1225-4614 · eISSN: 2288-890X
http://jkas.kas.org

Shock Acceleration Model with Postshock Turbulence for Giant Radio Relics

Hyesung Kang

Department of Earth Sciences, Pusan National University, 2 Busandaehak-ro, Geumjeong-gu, Busan 46241, Korea
hskang@pusan.ac.kr

Received May 9, 2017; accepted June 13, 2017

Abstract: We explore the shock acceleration model for giant radio relics, in which relativistic electrons are accelerated via diffusive shock acceleration (DSA) by merger-driven shocks in the outskirts of galaxy clusters. In addition to DSA, turbulent acceleration by compressive MHD modes downstream of the shock are included as well as energy losses of postshock electrons due to Coulomb scattering, synchrotron emission, and inverse Compton scattering off the cosmic background radiation. Considering that only a small fraction of merging clusters host radio relics, we favor a reacceleration scenario in which radio relics are generated preferentially by shocks encountering the regions containing low-energy ($\gamma_{\rm e} \lesssim 300$) cosmic ray electrons (CRe). We perform time-dependent DSA simulations of spherically expanding shocks with physical parameters relevant for the Sausage radio relic, and calculate the radio synchrotron emission from the accelerated CRe. We find that significant level of postshock turbulent acceleration is required in order to reproduce broad profiles of the observed radio flux densities of the Sausage relic. Moreover, the spectral curvature in the observed integrated radio spectrum can be explained, if the putative shock should have swept up and exited out of the preshock region of fossil CRe about 10 Myr ago.

Key words: acceleration of particles — cosmic rays — galaxies: clusters: general — shock waves

1. Introduction

The Sausage relic is a giant radio relic detected in the outskirts of the merging cluster CIZA J2242.8+5301 located at the redshift, $z = 0.188$ (van Weeren et al. 2010). It is an arc-like radio structure whose spectral index increases from the edge of the relic toward the cluster center. Its volume-integrated radio spectrum has a power-law form with a steep spectral curvature above ~ 2 GHz (Stroe et al. 2013, 2014). In van Weeren et al. (2010), the observed radio spectrum at the relic edge was interpreted as a power-law with slope, $\alpha_{\rm sh} \approx 0.6$, which can be translated into a 'radio Mach number', $M_{\rm rad} = [(3 + 2\alpha_{\rm sh})/(2\alpha_{\rm sh} - 1)]^{1/2} \approx 4.6$, based on the diffusive shock acceleration (DSA) model. On the other hand, the Mach number inferred from the Suzaku X-ray observations of Akamatsu et al. (2015) indicates a much lower 'X-ray Mach number', $M_{\rm X} = 2.7^{+0.7}_{-0.4}$. However, recent radio observations by Stroe et al. (2016) showed that the spectral index between 153 and 608 MHz may be fitted by $\alpha^{608}_{153} \approx 0.7$ slightly downstream of the hypothesized shock location, if we ignore the flattest point with $\alpha^{608}_{153} \approx 0.54$ near the relic edge (see Figure 3 below). This gives a much lower radio Mach number, $M_{\rm rad} \approx 3.3$, which compares better with $M_{\rm X}$.

The spectral steepening at high frequencies in the observed integrated spectrum, J_ν, of the Sausage relic is not consistent with a single power-law energy spectrum of relativistic electrons accelerated by a steady planar shock (Stroe et al. 2014, 2016). So Kang & Ryu (2016) suggested that such spectral curvature could be explained, if the relic is generated by a shock that sweeps through a finite-size cloud with preexisting cosmic ray electrons (CRe). Lack of seed electrons outside the cloud results in softening of the volume-integrated electron spectrum beyond radiative cooling alone. Moreover, it was pointed out that the ubiquitous presence of radio galaxies, AGN relics and radio phoenix implies that the intracluster medium (ICM) may contain *fossil* CRe left over from radio jets (Ensslin 1999; Slee et al. 2001; Clarke et al. 2013; Pinzke et al. 2013; de Gasperin et al. 2015; Kang 2016a).

In addition to the integrated spectrum, radio flux density, S_ν, can be used to constrain the shock model parameters such as the shock speed and magnetic field strength. The transverse length scale of the radio relic at high frequencies, for instance, is related to the cooling length of the electrons with synchrotron peak frequency, $\nu_{\rm peak} \approx 0.3(3eB/4\pi m_e c)\gamma_e^2$ (in *cgs* units):

$$\Delta l_{\rm cool} = t_{\rm rad}(\gamma_e)\cdot u_{2,3}$$
$$\approx 100\ {\rm kpc}\cdot u_{2,3}\cdot Q\cdot\left[\frac{\nu_{\rm obs}(1+z)}{0.63{\rm GHz}}\right]^{-1/2}, \quad (1)$$

where $t_{\rm rad}$ is the radiative energy loss time scale of CRe, $u_{2,3} = u_2/10^3$ km s^{-1} is the downstream flow speed, $\nu_{\rm obs}$ is the observation frequency and z is the redshift of the host cluster (Kang 2016a). Here, the factor Q is defined as

$$Q(B,z) \equiv \left[\frac{(5\ \mu{\rm G})^2}{B^2 + B_{\rm rad}(z)^2}\right]\left(\frac{B}{5\ \mu{\rm G}}\right)^{1/2}, \quad (2)$$

Corresponding author: H. Kang

where $B_{\rm rad} = 3.24\,\mu{\rm G}(1+z)^2$ accounts for energy losses due to inverse Compton (iC) scattering off the cosmic background radiation and B is expressed in units of μG (Kang 2011). Besides $\Delta l_{\rm cool}$, radio flux density profiles projected in the sky plane are also affected by the geometrical shape of the downstream volume and the viewing orientation (see Figure 1 of Kang 2015).

In Kang (2016b; Paper I), we attempted to reproduce the observed radio flux density profiles and the integrated spectrum by a reacceleration model in which a shock of sonic Mach number, $M_s \approx 3$, sweeps through a finite-sized cloud with a preexisting population of CRe, $f_{\rm pre} \propto p^{-s}\exp[-(p/p_{e,c})^2]$ with $s = 4.1$. A few shortcomings of this scenario are (1) the preexisting CRe is required to have a flat energy spectrum with high cutoff energy ($\gamma_{e,c} = p_{e,c}/m_e c \approx 3-5\times10^4$), (2) the dimension of the pre-shock region with such CRe should be as large as ~ 400 kpc across the width of the relic and ~ 2 Mpc along the length of the relic, and (3) the adopted temperatures of the preshock and postshock region, $kT_1 = 3.4$ keV and $kT_2 = 10.7-13.1$ keV are higher than the observed values, $kT_{1,\rm obs} = 2.7^{+0.7}_{-0.4}$ keV and $kT_{2,\rm obs} = 8.5^{+0.8}_{-0.6}$ keV (Akamatsu et al. 2015), respectively. Hereafter,the subscripts 1 and 2 identify the upstream and downstream states of a shock, respectively.

The first and second requirements may be considered somewhat unrealistic, because CRe with $\gamma_{e,c} > 3\times10^4$ cool radiatively in short cooling times ($t_{\rm rad} < 30$ Myr) in μG-level magnetic fields. So it would be challenging to maintain or replenish CRe with such a flat energy spectrum over such a large preshock volume (possibly from radio jets or lobes from AGNs.) On the other hand, the third requirement of high temperatures (i.e., large u_2) is necessary to reproduce the broad length scale of spectral steepening, $u_2 t_{\rm rad} \sim 150$ kpc, in the postshock flow (Donnert et al 2016).

Alternatively, we could increase the postshock cooling length by introducing an additional acceleration process such as turbulent acceleration behind the shock (e.g., Kang et al. 2017). In merging clusters, turbulence can be injected into the ICM and cascade down to smaller scales, which may further energize relativistic electrons via stochastic Fermi II acceleration, resulting in radio halos (Brunetti & Jones 2014). Similarly, MHD/plasma turbulence can be generated at collisionless shocks, which could lead to turbulent acceleration of CRe in the postshock region of radio relics. Fujita et al. (2015) suggested that reacceleration of postshock electrons through resonant interactions with strong Alfvénic turbulence could produce radio spectra harder than predicted by the DSA. We do not consider such interaction here, since Alfvénic turbulence is expected to become highly anisotropic on small scales and thus inefficient in resonant scattering of CRe (e.g., Yan & Lazarian 2002). As in Kang et al. (2017), we will consider electron interactions with the compressive fast modes of MHD turbulence via the transit time damping (TTD) resonance, which is thought be the dominant process in high beta ($\beta_p = P_g/P_B \sim 50-100$) ICM plasma (Brunetti & Lazarian 2007, 2011).

In this study, we explore the reacceleration model for the Sausage relic, which differs from the models considered in Paper I in the following aspects: (1) Preexisting CR electrons consist of only low energy electrons with $\gamma_e \lesssim 300$ that have long cooling times ($t_{\rm rad} \gtrsim 3.5$ Gyr), so they merely provide seed electrons to be injected to the Fermi I process. (2) The radio spectral index of the relic at the shock location is determined by the shock Mach number, $M_{\rm s} \sim 3$, instead of the energy spectrum of preexisting CRe (i.e. s and $\gamma_{e,c}$). (3) The shock-accelerated electrons are further accelerated by the Fermi II process due to postshock turbulence, delaying the spectral aging of CRe behind the shock.

In the next section, the numerical simulations and the shock models are described. The comparison of our results with observations is presented in Section 3, followed by a brief summary in Section 4.

2. NUMERICAL CALCULATIONS

The numerical setup for our DSA simulations was described in detail in Paper I and Kang et al. (2017). Some basic features are repeated here in order to make this paper self-contained.

2.1. DSA Simulations for 1D Spherical Shocks

We assume that the Sausage relic can be represented by a wedge-like patch of a spherical shell shown in Figure 1 of Kang (2015), whose depth along the line-of-sight is specified by the extension angle ψ. The spherical shell that contains radio-emitting electrons is assumed to be generated by a spherically expanding shock and its downstream volume.

We follow the electron DSA along with radiative cooling and postshock turbulent acceleration by solving the diffusion-convection equation in the one-dimensional (1D) spherically symmetric geometry:

$$\frac{\partial g_{\rm e}}{\partial t} + u\frac{\partial g_{\rm e}}{\partial r} = \frac{1}{3r^2}\frac{\partial (r^2 u)}{\partial r}\left(\frac{\partial g_{\rm e}}{\partial y} - 4g_{\rm e}\right) + \frac{1}{r^2}\frac{\partial}{\partial r}\left[r^2\kappa(r,p)\frac{\partial g_{\rm e}}{\partial r}\right] + p\frac{\partial}{\partial y}\left[\frac{D_{pp}}{p^3}\left(\frac{\partial g_{\rm e}}{\partial y} - 4g_{\rm e}\right)\right] + p\frac{\partial}{\partial y}\left(\frac{b}{p^2}g_{\rm e}\right), \quad (3)$$

where $f_e(r,p,t) = g_e(r,p,t)p^{-4}$ is the pitch-angle-averaged phase space distribution function for CRe, $u(r,t)$ is the flow velocity, $y = \ln(p/m_e c)$, m_e is the electron mass, and c is the speed of light (Skilling 1975). Here r is the radial distance from the cluster center.

We adopt a Bohm-like spatial diffusion coefficient, $\kappa(p) = \kappa_N \cdot (p/m_e c)$ for relativistic electrons, where the normalization factor, $\kappa_N = k_{\rm B}\cdot m_e c^3/(3eB) = k_{\rm B}\cdot 1.7\times10^{19}{\rm cm^2 s^{-1}}/B_{\mu{\rm G}}$, with $B_{\mu{\rm G}}$ expressed in units of μG. The numerical factor, $k_{\rm B}$, depends on the strength of turbulent magnetic fields, δB and becomes $k_{\rm B} = 1$ for Bohm diffusion that represents particle diffusion in completely random fluctuating fields.

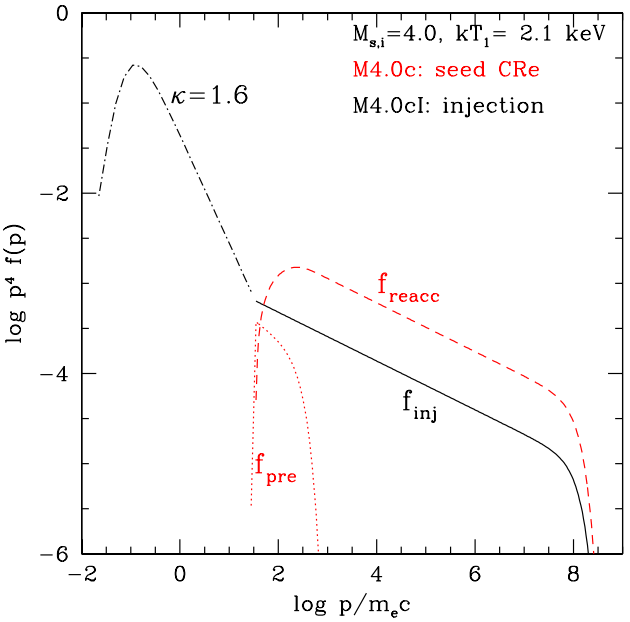

Figure 1. Electron distribution function at the shock position, $f_{\rm inj}$ (black solid line) in the *in situ* injection model and $f_{\rm reacc}$ (red dashed) in the reacceleration model. The red dotted line shows the spectrum of preexisting seed CRe, $f_{\rm pre}$, while the black dot-dashed line shows the κ-distribution with $\kappa = 1.6$.

The electron energy loss term, $b(p) = \dot{p}_{\rm Coul} + \dot{p}_{\rm sync+iC}$, accounts for Coulomb scattering, synchrotron emission, and iC scattering off the cosmic background radiation (e.g., Sarazin 1999).

Here we explore a scenario in which the postshock electrons gain energy from turbulent waves via Fermi II acceleration, thus abating spectral aging downstream of the shock. As in Kang et al. (2017), we consider a simple model based on TTD resonance with compressive fast-mode MHD turbulence, since that is likely to be the most efficient turbulent acceleration process in the ICM (Brunetti & Lazarian 2007, 2011). The momentum diffusion coefficient for TTD resonance can be modeled as

$$D_{pp} = \frac{p^2}{4\,\tau_{\rm acc}}, \tag{4}$$

where $\tau_{\rm acc}$ is an effective acceleration time scale for turbulent acceleration. In order to model the decay of turbulence behind the shock, we assume the turbulent acceleration time increases behind the shock over the scale $r_{\rm dec}$ as

$$\tau_{\rm acc} = \tau_{\rm acc,0} \cdot \exp\left[\frac{(r_s - r)}{r_{\rm dec}}\right] \tag{5}$$

with, in most of our simulations, $\tau_{\rm acc,0} \approx 10^8$ yr and $r_{\rm dec} \approx 100$ kpc.

2.2. Injection versus Reacceleration Model

In this study, we consider two kinds of DSA models: (1) in the *injection model*, suprathermal particles are generated via plasma kinetic processes near the shock and injected into the Fermi I process at the shock, and (2) in the *reacceleration model*, preexisting low energy CRe are injected into the Fermi I process. In both models, the injected electrons are accelerated via DSA at the shock, and then they cool radiatively while being accelerated via turbulent acceleration behind the shock.

In the *injection model*, the electron population at the shock location (r_s), which is injected *in situ* from the background suprathermal population and then accelerated by DSA, can be modeled as

$$f_{\rm inj}(r_s, p) = f_N \left(\frac{p}{p_{\rm inj}}\right)^{-q} \exp\left[-\left(\frac{p}{p_{\rm eq}}\right)^2\right], \tag{6}$$

where f_N, $q = 4M_{\rm s}^2/(M_{\rm s}^2 - 1)$, $p_{\rm inj}$, and $p_{\rm eq}$ are the normalization factor, the standard test-particle DSA power-law slope, the injection momentum, and the cutoff momentum, respectively. The injection momentum represents the low momentum boundary above which particles have mean free paths large enough to cross the shock transition and thus participate in the Fermi I acceleration process. Here, we adopt a simple model in which the electron injection depends on the shock strength as $p_{\rm inj} \approx (6.4/\sigma) m_p u_s$ (where $\sigma = \rho_2/\rho_1$ is the shock compression ratio), in effect, resulting in $p_{\rm inj} \sim 150 p_{\rm th,e}$. The cutoff momentum can be estimated from the condition that the DSA acceleration rate balances the synchrotron/iC loss rate (Kang 2011). For typical parameters for the ICM shocks, $u_s \sim 3 \times 10^3$ km s^{-1} and $B_1 \sim 1$ μG, if we assume Bohm diffusion, it becomes $p_{\rm eq}/m_{\rm e}c \sim 10^8$.

The factor f_N depends on the suprathermal electron population in the background plasma, which is assumed to be energized via kinetic plasma processes at the shock and form a κ-distribution, rather than a Maxwellian distribution (Pierrard & Lazar 2010). The κ index is expected to depend on the shock parameters such as the obliquity angle and sonic and Alvénic Mach numbers, in addition to plasma parameters of the background medium. For instance, the electron energy spectrum measured *in situ* in the solar wind near the Earth's orbit can be fitted with the κ-distribution with $\kappa \sim 2-5$ (Pierrard & Lazar 2010). Here we adopt a somewhat flatter value of $\kappa \sim 1.6$ to maximize the electron injection rate. Figure 1 illustrates the κ-distribution (dot-dashed line) for $p < p_{\rm inj}$ and $f_{\rm inj}(r_s, p)$ (solid line) for $p > p_{\rm inj}$ in one of the models considered below. For $p \gg p_{\rm th,e}$, the κ-distribution can be approximated as $f_\kappa \propto p^{-2(\kappa+1)}$, so the amplitude f_N becomes smaller for a larger value of κ. For example, the factor f_N for $\kappa = 2.5$ is smaller by a factor of about 200 than that for $\kappa = 1.6$.

In the case of the *reacceleration model*, the preexisting seed CRs are assumed to have a power-law spectrum with exponential cutoff as follows:

$$f_{\rm pre}(p) = f_o \cdot p^{-s} \exp\left[-\left(\frac{p}{p_{e,c}}\right)^2\right], \tag{7}$$

where the slope $s = 4.6$ and the cutoff $\gamma_{e,c} = 300$ are

Table 1
Model Parameters for the Sausage Radio Relic

Model	$M_{\rm s,i}$	kT_1 (keV)	B_1 (μG)	$L_{\rm cloud}$ (kpc)	$t_{\rm exit}$ (Myr)	$t_{\rm obs}$ (Myr)	$M_{\rm s,obs}$	$kT_{2,\rm obs}$ (keV)	$u_{\rm s,obs}$ (km s^{-1})	N	remarks
M3.5a	3.5	2.5	1	420	144	155	2.97	9.0	2.4×10^3	1.6×10^{-4}	seed CRe
M3.5b	3.5	2.5	1	485	167	177	2.93	8.8	2.4×10^3	1.6×10^{-4}	seed CRe
M3.5c	3.5	2.5	1	581	200	214	2.86	8.5	2.3×10^3	1.6×10^{-4}	seed CRe
M4.0a	4.0	2.1	1	451	144	159	3.34	9.1	2.5×10^3	1.2×10^{-4}	seed CRe
M4.0b	4.0	2.1	1	520	167	180	3.28	8.9	2.4×10^3	1.2×10^{-4}	seed CRe
M4.0c	4.0	2.1	1	624	200	211	3.21	8.6	2.4×10^3	1.2×10^{-4}	seed CRe
M4.0cI	4.0	2.1	1	—	200	211	3.21	8.6	2.4×10^3	$\kappa=1.6$	injection
M4.0cB	4.0	2.1	2.5	624	200	211	3.21	8.6	2.4×10^3	1.2×10^{-4}	stronger B
M4.0cN	4.0	2.1	1	624	200	211	3.21	8.6	2.4×10^3	1.2×10^{-4}	No TA

$M_{\rm s,i}$: initial shock Mach number at the onset of the simulations ($t_{\rm age}=0$)
kT_1: preshock temperature
B_1: preshock magnetic field strength
$L_{\rm cloud}$: size of the cloud with preexisting CR electrons
$t_{\rm exit}$: shock age when the shock exit out of the cloud with preexisting electrons
$t_{\rm obs}$: shock age when the simulated results match the observations
$M_{\rm s,obs}$: shock Mach number at $t_{\rm obs}$
$kT_{2,\rm obs}$: postshock temperature at $t_{\rm obs}$
$u_{\rm s,obs}$: shock speed at $t_{\rm obs}$
$N=P_{\rm CRe}/P_{\rm g}$: the ratio of seed CR electron pressure to gas pressure
The subscripts 1 and 2 indicate the preshock and postshock quantities, respectively.

adopted for all models considered here (see the red dotted line in Figure 1). However, the exact shape of $f_{\rm pre}(p)$ is not important, because the only significant role of these low-energy CRe is to provide seed particles to be injected to the DSA process. Note that the electrons with $\gamma_{e,c}<300$ cool on time scales longer than 3.5 Gyr, so they could represent fossil electrons in the ICM that are left over from AGN jets ejected early on. The normalization factor, f_o, can be parameterized by the ratio of the pressure of preexisting CRe to the gas pressure in the preshock region, $N\equiv P_{\rm CRe,1}/P_{\rm gas,1}\propto f_o$ for a given set of s and $p_{e,c}$. In the models considered here, typically, $N\sim10^{-4}$ produce the radio flux profiles that match the amplitude of observed flux in the Sausage relic.

The reaccelerated population of $f_{\rm pre}(p)$ at the shock location can be calculated by

$$f_{\rm reacc}(r_s,p)=q\cdot p^{-q}\int_{p_{\rm inj}}^{p}p'^{q-1}f_{\rm pre}(p')dp' \qquad (8)$$

(Drury 1983). Note that if the DSA slope, q, is flatter (smaller) than the slope, s, of the preexisting population, the downstream energy spectrum does not carry any memory of the upstream spectrum other than its amplitude. As can be seen in the red dashed and black solid lines in Figure 1, both $f_{\rm reacc}(r_s,p)$ and $f_{\rm inj}(r_s,p)$ have the same power-law form.

Since the time scale for DSA at the shock is much shorter than the electron cooling time scale, we can assume that electrons are accelerated almost *instantaneously* to $p_{\rm eq}$ at the shock front. Moreover, the minimum diffusion length scale to obtain convergent solutions in simulations for diffusion-convection equation is much smaller than the typical downstream cooling length of $\sim$ 100 kpc. Taking advantage of such disparate scales, we adopt *analytic* solutions for the electron spectrum *at the shock location* as $f(r_s,p)=f_{\rm inj}(r_s,p)$ or $f_{\rm reacc}(r_s,p)$, while Equation (3) is solved outside the shock. So, basically we track energy losses and turbulent acceleration of electrons behind the shock, while the DSA analytic solutions are applied to the zone containing the shock.

2.3. Shock Parameters

It is not well understood how merger-driven shocks evolve dynamically as they propagate in the cluster periphery. In a major binary merger, shocks are launched after core passage of the two subclumps and propagate beyond the virial radius of the newly formed cluster (van Weeren et al. 2011). It is expected that in general shock speeds increase during the initial launch period and may decrease later during the expansion stage. In a realistic cluster merger, however, the merger is likely to involve subsequent infall of more subclumps along the filaments connected with the cluster. So the dynamical evolution of a merger shock can be quite complex (e.g., Paul et al. 2011).

Here we assume that the shock dynamics can be approximated by a self-similar blast wave that propagates through the isothermal ICM with the density profile of $n_{\rm H}=10^{-4}$ cm$^{-3}(r/0.8{\rm Mpc})^{-2}$, where $n_{\rm H}$ is the number density of hydrogen atom. So the shock radius and velocity evolves roughly as $r_s\propto t^{2/3}$ and $u_s\propto t^{-1/3}$, respectively, where t is the time since the point explosion for the spherical blast wave (e.g., Ryu & Vishniac 1991). During the simulation time period of $\sim$ 200 Myr, the model shock speed decreases by a factor of $\lesssim1.3$.

The ICM temperature upstream and downstream

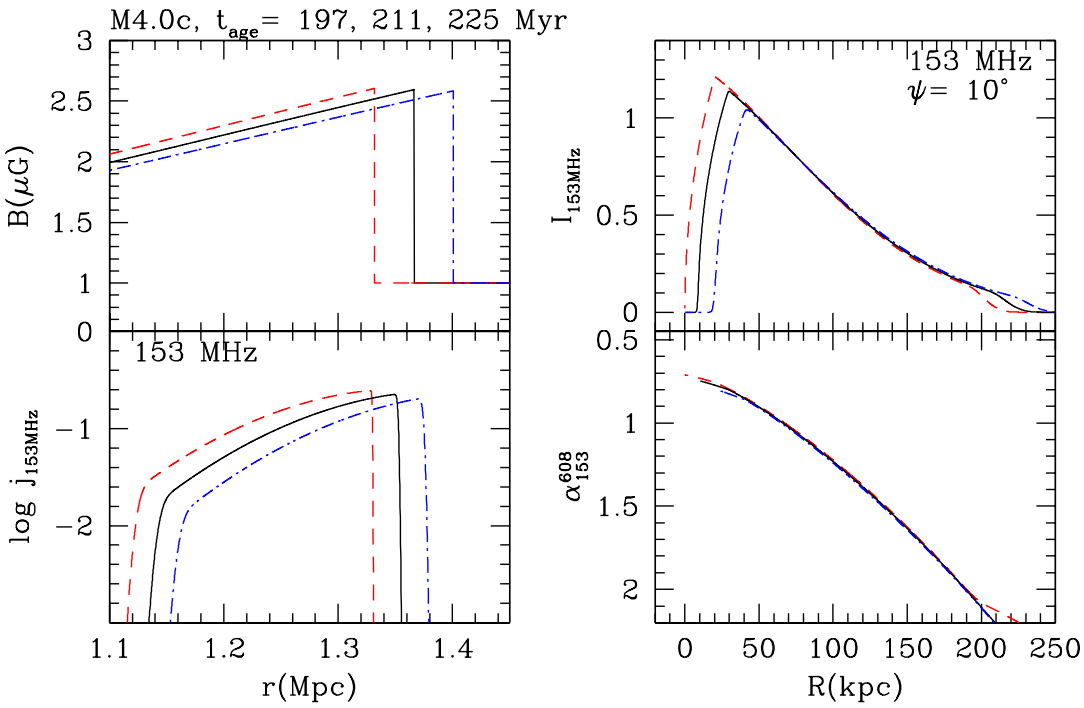

Figure 2. Results for the fiducial model M4.0c at $t_{\rm age}$ = 197 (red dashed lines), 211 (black solid), and 225 Myr (blue dot-dashed). Left: magnetic field strength, $B(r)$ and synchrotron emissivity, $j_{153\rm MHz}(r)$, where r is the radial distance from the cluster center in units of Mpc. Right: surface brightness, $I_{153\rm MHz}(R)$, and spectral index, α^{608}_{153} between 153 and 608 MHz, where R is the projected distance behind the shock in units of kpc.

of the relic edge is observed to be $kT_1 = 2.7^{+0.7}_{-0.4}$ keV and $kT_2 = 8.5^{+0.8}_{-0.6}$ keV, respectively, which indicates the sonic Mach number of $M_s \approx 2.7$ (Akamatsu et al. 2015). Since the shock speed decreases in time in our model, we consider two values for the initial shock Mach number, $M_{\rm s,i} = 3.5$ and 4.0, and two values for the preshock temperature, $kT_1 = 2.5$ keV and 2.1 keV, respectively. Table 1 shows the model parameters for the DSA simulations considered here.

At the onset of the simulations ($t = t_i$), the initial shock speed, $u_{\rm s,i}$ is specified by $M_{\rm s,i}$ and kT_1, while the shock location is assumed to be $r_{\rm s,i} = 0.8$ Mpc. This fixes the initial time t_i when the shock encounters the cloud of preexisting CRe, and the scaling factors for the similarity solution, ρ_o, u_o, and t_o. We define the "shock age", $t_{\rm age} \equiv t - t_i$, as the time since the onset of the simulations.

As in Paper I, in order to reproduce the spectral steepening around 2 GHz, we assume that, in the reacceleration model, at the onset of the simulations the shock encounters a cloud of size $L_{\rm cloud}$ containing preexisting seed CRs, and then exits out of it at $t_{\rm exit}$. So the size $L_{\rm cloud}$ affects the postshock profiles of radio flux densities. The 'time of observation', $t_{\rm obs}$, is then chosen when both the simulated brightness profiles and the integrated spectra become consistent with the observations reported by Stroe et al. (2016). Between the exit time, $t_{\rm exit}$, and $t_{\rm obs}$, the shock sweeps the region devoid of preexisting CRe, which results in steepening of the volume-integrated electron energy spectrum. As a result, the elapsed period of $(t_{\rm obs} - t_{\rm exit}) \approx 10 - 15$ Myr controls the spectral curvature of the integrated radio spectrum.

The fiducial value of the preshock magnetic field strength is set to be $B_1 = 1\mu$G, which is assumed to be uniform in the upstream region. As in Paper I, the postshock magnetic field strength is modeled as $B_2(t) = B_1\sqrt{1/3 + 2\sigma(t)^2/3} \approx 2.5 - 2.7\mu$G, which decreases slightly because the shock compression ratio, $\sigma(t)$, decreases in time in response to shock evolution. For the downstream region ($r < r_s$), we assume a simple model in which the magnetic field strength scales with the gas pressure as $B_{\rm dn}(r,t) = B_2(t)\cdot[P(r,t)/P_2(t)]^{1/2}$, where $P_2(t)$ is the gas pressure immediately behind the shock (see Figure 2).

We adopt the model naming convention as in Table 1, where the number after the first letter 'M' corresponds to $M_{\rm s,i}$. This is followed by a sequence label (a, b, c) as the size of the cloud containing preexisting CRe, $L_{\rm cloud}$, increases. The M4.0c model is the reacceleration model with fossil CRe with $M_{\rm s,i} = 4.0$ and $L_{\rm cloud} = 624$ kpc. The M4.0cI model is the injection model in which only *in situ* injection from background suprathermal electrons is included, while the M4.0cB model adopts a preshock magnetic field strength higher than that of the rest of the models. In M4.0cI, the *in situ* injection is turned on at the onset of the simulation, and then it is turned off at $t_{\rm exit} = 200$ Myr to create a spectral curvature at high frequencies. In the M4.0cN model, turbulent acceleration is turned off to

demonstrate its effects on the postshock spectral aging.

The eighth and ninth columns of Table 1 show the shock Mach number and the postshock temperature at $t_{\rm obs}$: $M_{\rm s,obs} = 2.9 - 3.3$ and $kT_{2,\rm obs} = 8.5 - 9.1$ keV, which are reasonably consistent with the X-ray observations reported by Akamatsu et al. (2015).

We note here that $M_{\rm X}$ inferred from X-ray observations could be lower than $M_{\rm radio}$ estimated from the radio spectral index, since a radio relic may be associated with multiple shocks. According to mock observations of cluster shocks formed in structure formation simulations, X-ray observations tend to pick up shocks with lower $M_{\rm s}$ along a given line-of-sight, while radio emissions come preferentially from shocks with higher $M_{\rm s}$ (e.g., Hong et al. 2015). In the case of the Toothbrush relic, it was shown that $M_{\rm s} \approx 3.0$ is required to reproduce the radio data, while the X-ray data indicate $M_{\rm X} \approx 1.2 - 1.5$ (Kang et al. 2017).

Finally, the eleventh column shows, $N \approx 10^{-4}$, the ratio of the pressure of preexisting CRe to that of the upstream gas that can generate radio flux densities consistent with the observations reported by Stroe et al. (2016).

3. RESULTS OF DSA SIMULATIONS

Figure 2 shows the DSA simulation results for the M4.0c model at three epochs: just before the shock exits out of the cloud at $t_{\rm exit} \approx 200$ Myr (red dashed lines), at the time of observation, $t_{\rm obs} = 211$ Myr (black solid), and at $t_{\rm age} = 225$ Myr (blue dot-dashed). The upper left panel shows the profiles of the magnetic field strength, which contain a discontinuous jump at the shock location, $r_{\rm s}(t) = 1.33 - 1.4$ Mpc. Note that the shock expands radially outward in the left-hand panels of Figure 2.

3.1. Surface Brightness and Spectral Index Profiles

Using the CRe energy spectrum and the magnetic field strength in the model DSA simulations, we first calculate the synchrotron emissivity $j_\nu(r)$ of each spherical shell. The lower left panel of Figure 2 demonstrates that the outermost edge of the synchrotron emissivity at 153 MHz, $j_{153\rm MHz}(r)$, lags behind the shock location after the shock moves out of the cloud at $t_{\rm exit}$.

The radio surface brightness, $I_\nu(R)$, is calculated by integrating $j_\nu(r)$ along a given line-of-sight, where a wedge-like postshock volume of radio-emitting electrons is adopted, as in Figure 1 of Kang (2015). Here R is the distance behind the projected shock edge in the plane of the sky. This volume is specified by the extension angle, ψ, which is assumed to be about 10° in the case of the Sausage relic (e.g., van Weeren et al. 2010; Kang et al. 2012). The upper right panel of Figure 2 shows $I_{153\rm MHz}(R)$ at 153 MHz (in arbitrary units), using $\psi = 10^\circ$. Note that the shock faces to the left in the right-hand panels of Figure 2, so the region of $R < 0$ is the preshock region. Again, one can see that the edge of the radio relic is located the behind the shock (at $R = 0$) after $t_{\rm exit}$. The spectral index profile, $\alpha_{153}^{608}(R)$ in the lower right panel is calculated with the ratio between $I_{153\rm MHz}(R)$ and $I_{608\rm MHz}(R)$.

In order to obtain beam-convolved flux density, the intensity $I_\nu(R)$ is smoothed by Gaussian smoothing with 51.7 kpc width (equivalent to $16.14''$) for 153 MHz and 13.4 kpc width (equivalent to $4.2''$) for 608 MHz. For the profile of the spectral index, $\alpha_{153}^{608}(R)$, both $I_{153\rm MHz}(R)$ and $I_{608\rm MHz}(R)$ are smoothed with the same width of 51.7 kpc.

Figure 3 shows the time evolution of $S_{153\rm MHz}(R)$, $S_{608\rm MHz}(R)$, and $\alpha_{153}^{608}(R)$ in the M4.0a, b, c models with different cloud size $L_{\rm cloud}$. The times of observation, $t_{\rm obs} = 159$, 180, and 211 Myr (black solid lines) are chosen for the M4.0a, b, c models, respectively. For each model, the results at the times earlier (red dashed lines) or later (blue dot-dashed lines) than $t_{\rm obs}$ are also shown for comparison. Since the shock slows down and moves out of the cloud of preexisting CRe at $t_{\rm exit}$ (given in Table 1), the amplitude of S_ν decreases in time.

The observed flux density at 153 MHz for a beam of dimensions $16.14'' \times 13.75''$ is $S_{153\rm MHz} \approx 0.014$ Jy at $R \approx 55$ kpc (Stroe et al. 2016). In Figure 3, the normalization factor of S_ν and its peak location are chosen so that the black solid lines match the observed data represented by the magenta solid circles. The amount of preexisting CRe needed to match the observed flux density corresponds to $N \approx 1.6 \times 10^{-4}$ (see Table 1).

Although the three models can reproduce reasonably well both $S_{153\rm MHz}(R)$ and $S_{608\rm MHz}(R)$, the M4.0c model (at 211 Myr) best fits the observed profile of $\alpha_{153}^{608}(R)$. So we take the M4.0c model as the 'fiducial' model in this discussion. In the M4.0a and M4.0b models, $L_{\rm cloud}$ is smaller, so the shock exits out of the cloud earlier, resulting in less spectral aging for $R > 150$ kpc at $t_{\rm obs}$, compared to the M4.0c model (see the bottom panels of Figure 3). Of course, if we were to choose a later epoch for $t_{\rm obs}$ for these two models, the spectral index profile would become more comparable to the observations. As we will show in Figure 5 below, however, the time interval of $t_{\rm obs} - t_{\rm exit}$ becomes longer in those cases, making the spectral curvature of the integrated radio spectrum much steeper than observed.

Note that we do not attempt to fit the flattest data for $\alpha_{153}^{608} \approx 0.54$ at $R \approx 0$ kpc. This allows us to choose a much smaller shock Mach number, i.e., $M_{\rm s,obs} \approx 3.2$ for the M4.0c model, instead of $M_{\rm radio} \approx 4.6$ suggested in earlier papers (e.g., van Weeren et al. 2010).

The right-hand panels of Figure 4 show the results at $t_{\rm obs} = 155$, 177, and 214 Myr for M3.5a, b, c models, respectively. The M3.5c model at $t_{\rm obs} = 214$ Myr seems to give the best fit to the observations. But the profiles of $\alpha_{153}^{608}(R) \gtrsim 0.8$ for $R < 80$ kpc are slightly steeper than the observed profile in these three models with $M_{\rm s,obs} = 2.9 - 3.0$.

The left-hand panels of Figure 4 compare the M4.0cB (stronger B_1, red dashed lines) with the M4.0c model. Stronger magnetic fields enhance the synchrotron emission and cooling, resulting in higher radio flux densities and a steeper profile of $\alpha_{153}^{608}(R)$. In the figure S_ν has been scaled by a factor 0.23 for the

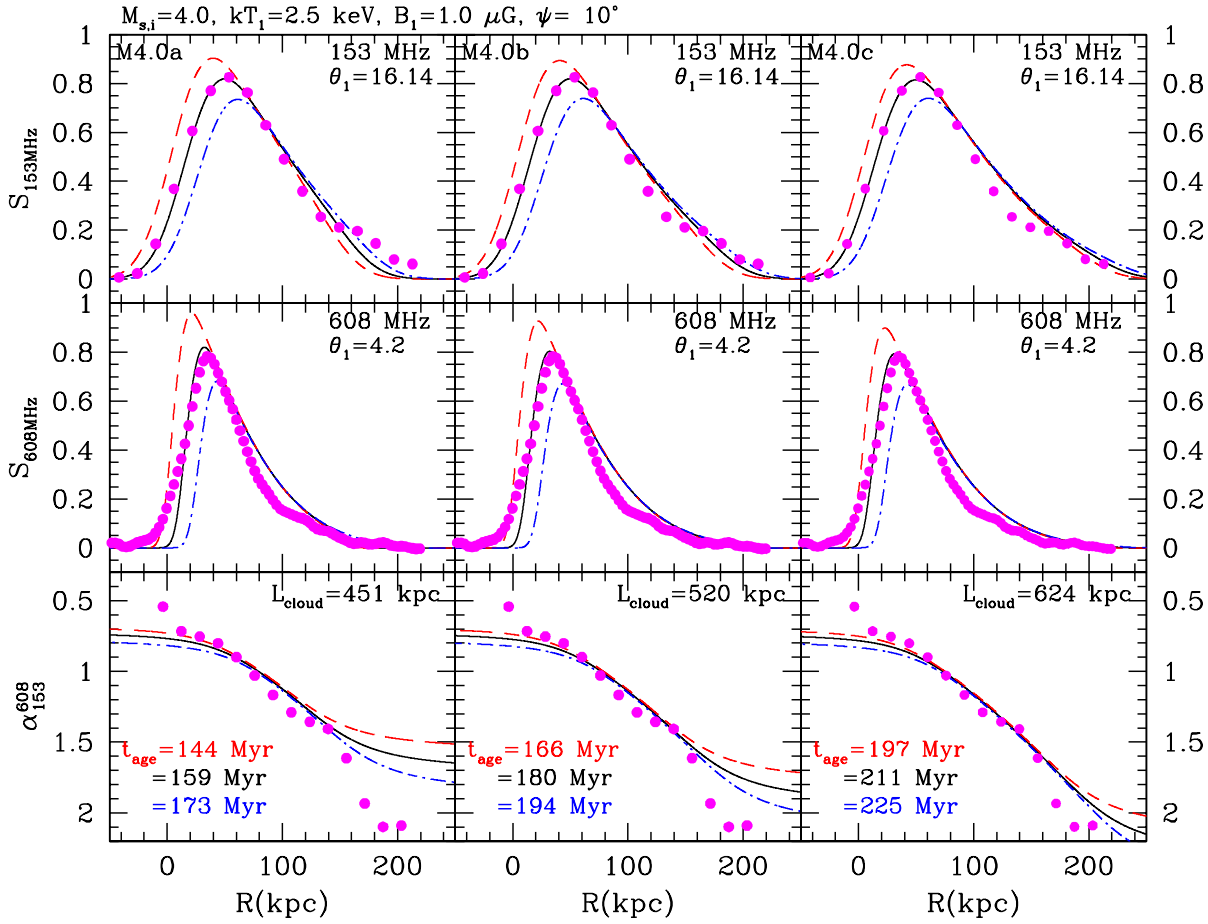

Figure 3. Beam convolved brightness profiles $S_\nu(R)$ at 153 MHz (top panels) and at 608 MHz (middle panels), and the spectral index α_{153}^{608} between the two frequencies (bottom panels) are plotted for three shock ages (red, black, and blue lines), as specified in the bottom panels. Here R is the projected distance behind the shock in units of kpc. The extension angle, $\psi = 10^\circ$, is adopted. The results are shown for the M4.0a model with $L_{\rm cloud} = 451$ kpc (left-hand panels), M4.0b model with $L_{\rm cloud} = 520$ kpc (middle panels), and M4.0c model with $L_{\rm cloud} = 624$ kpc (right-hand panels). The simulated brightness profiles, $I_\nu(R)$, are smoothed with Gaussian smoothing with 51.7 kpc (equivalent to the beam angle $\theta_1 = 16.14''$) for 153 MHz and with 13.4 kpc (equivalent to $\theta_1 = 3.42''$) for 608 MHz to be compared with the observed flux profiles of the Sausage relic reported by Stroe et al. (2016) (magenta filled circles).

M4.0cB model.

In the middle panels of Figure 4, the M4.0cI (injection only, blue dot-dashed lines) and M4.0cN (no turbulent acceleration, red dashed lines) are compared with the fiducial M4.0c model. As mentioned in Section 2.2, the normalization for the injection model depend on the value of the κ index for the suprathermal electrons in the background plasma (see Figure 1). With $\kappa = 1.6$ in M4.0cI, the peak value becomes $S_{153\rm MHz} \approx 0.018$ Jy, so the radio flux densities are scaled down by a factor of 0.77 for this model in order to compare them with the observational data in the figure. We note, however, a more realistic value would be $\kappa > 2$, so the amplitude of $S_{153\rm MHz}$ in the injection model might be much smaller than observed. In the M4.0cN model without turbulent acceleration, S_ν is smaller and α_{153}^{608} is steeper, compared to the M4.0c model.

Figures 3 and 4 show that the predictions of the M4.0c model convolved with appropriate beam widths are in reasonable agreement with the observations, providing that there exist fossil CRe with $N \approx 10^{-4}$ in the ICM. This exercise demonstrates that the profiles of observed radio flux density, $S_\nu(R)$, at multi frequencies can provide strong constraints on the model parameters for radio relics.

3.2. Integrated Spectrum

As shown in Paper I, the spectral curvature observed in the integrated radio spectrum of the Sausage relic cannot be reproduced by a simple DSA model for a steady planar shock. But it can be explained if we adopt two additional conditions for a finite size of the cloud with preexisting CRe. We note that in the *in situ* injection model (M4.0cI), the same kind of curvature can be created somewhat artificially by turning off the injection after $t_{\rm exit} = 200$ Myr.

Figure 5 shows the time evolution of the integrated spectrum, νJ_ν, for six different models. The red dashed

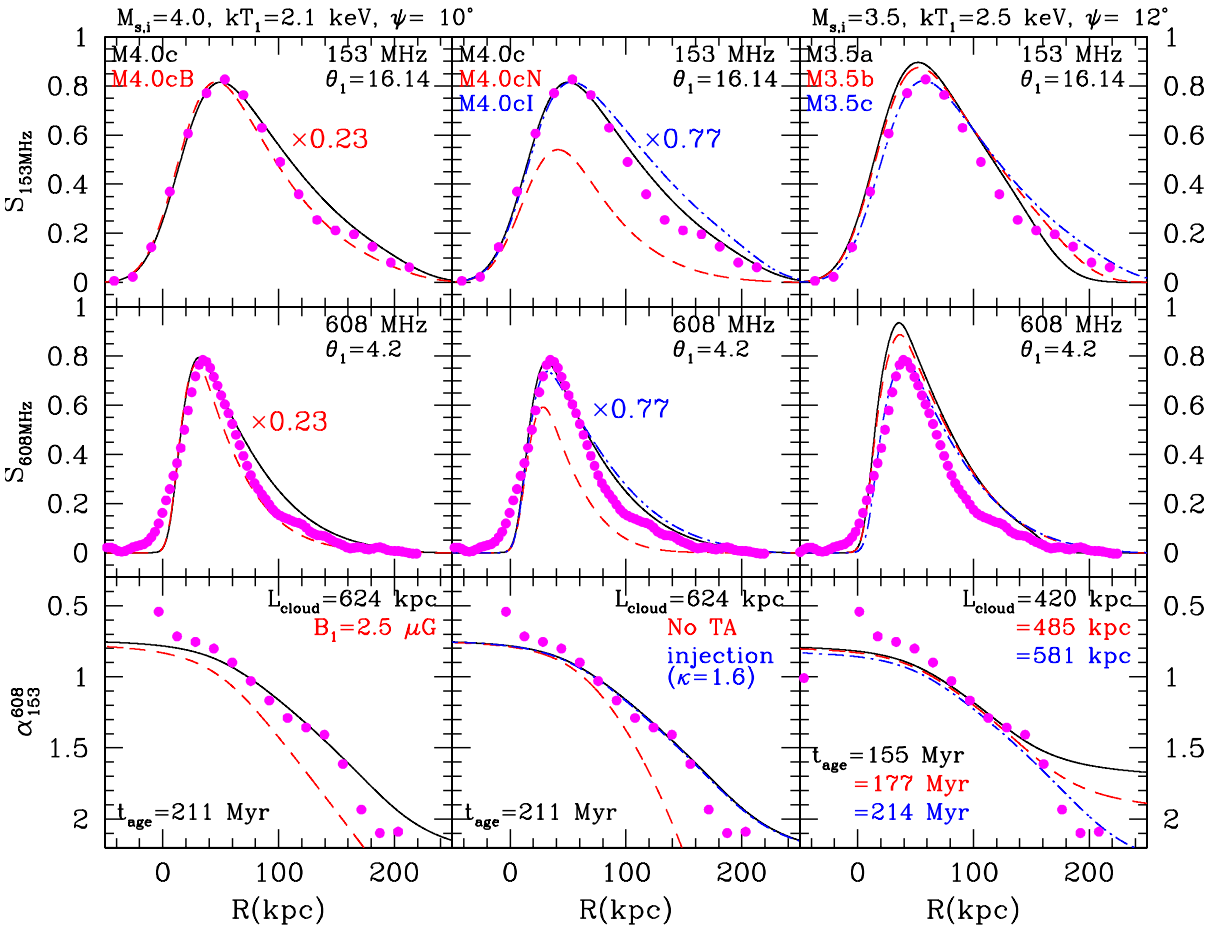

Figure 4. Same as Figure 2 except that the M4.0c and M4.0cB models with the extension angle $\psi = 10^\circ$ are compared in the left-hand panels, the M4.0c, M4.0cN, and M4.0cI models with $\psi = 10^\circ$ are compared in the middle panels, and the M3.5a, M3.5b, and M3.5c models with $\psi = 12^\circ$ are compared in the right-hand panels. The radio flux density, S_ν, is multiplied by a factor of 0.23 for M4.0cB and 0.77 for M4.0cI with respect to S_ν for the fiducial model, M4.0c.

lines for each model show the spectrum at the first epoch just before the shock exits out of the cloud. They follow roughly the predictions based on the postshock radiative cooling, i.e., steepening of J_ν from $\nu^{-\alpha_s}$ to $\nu^{-(\alpha_s+0.5)}$ at ∼GHz. Such a description is only approximate here, because additional turbulent acceleration operates in the postshock region.

Then the green dot-dashed lines, black solid lines, magenta dot-long dashed lines, and blue long dashed lines present the spectra with progressively steeper curvatures at four later epochs in chronological order. The open magenta squares and the error bars are observational data taken from Table 3 of Stroe et al. (2016). Basu et al. (2016) calculated the amount of the Sunyaev-Zeldovich (SZ) decrement in the observed radio flux for several well-known radio relics, based on models for the ICM electron density profile and the radio flux profile. Although we know such predictions depend sensitively on model details, we adopt their estimates for the SZ contamination factor for the Sausage relic given in their Table 1. Then, the SZ correction factors, F, for the fluxes at 16 GHz and 30 GHz are about 1.1 and 1.96, respectively. The two solid circles in each panel of Figure 5 correspond to the flux levels so-corrected at the two highest frequencies.

Note that Stroe et al. (2016) suggested that the observed spectrum could be fitted by a broken power-law: $\alpha = 0.90 \pm 0.04$ below 2 GHz and $\alpha = 1.77 \pm 0.13$ above 2 GHz. The black solid lines at $t_{\rm obs}$ for each model are chosen as the best fits to the observed spectrum in the range of $1 - 3$ GHz. All six models seem to generate similar integrated spectra, although the simulated profiles of $\alpha_{153}^{608}(R)$ are rather different as shown in Figures 3 and 4. Considering that the observation errors in the flux data is only 10% for $\nu \lesssim 3$ GHz, it seems somewhat difficult to fit very well the observational data both below and above 1 GHz simultaneously with our model predictions. We conclude the fiducial model M4.0c is the best case, in which the predictions for both $\alpha_{153}^{608}(R)$ and νJ_ν are in reasonable agreement with the observations.

Note that in previous studies including Paper I the integrated spectrum was often presented in the form of J_ν typically over four orders of magnitudes, so it

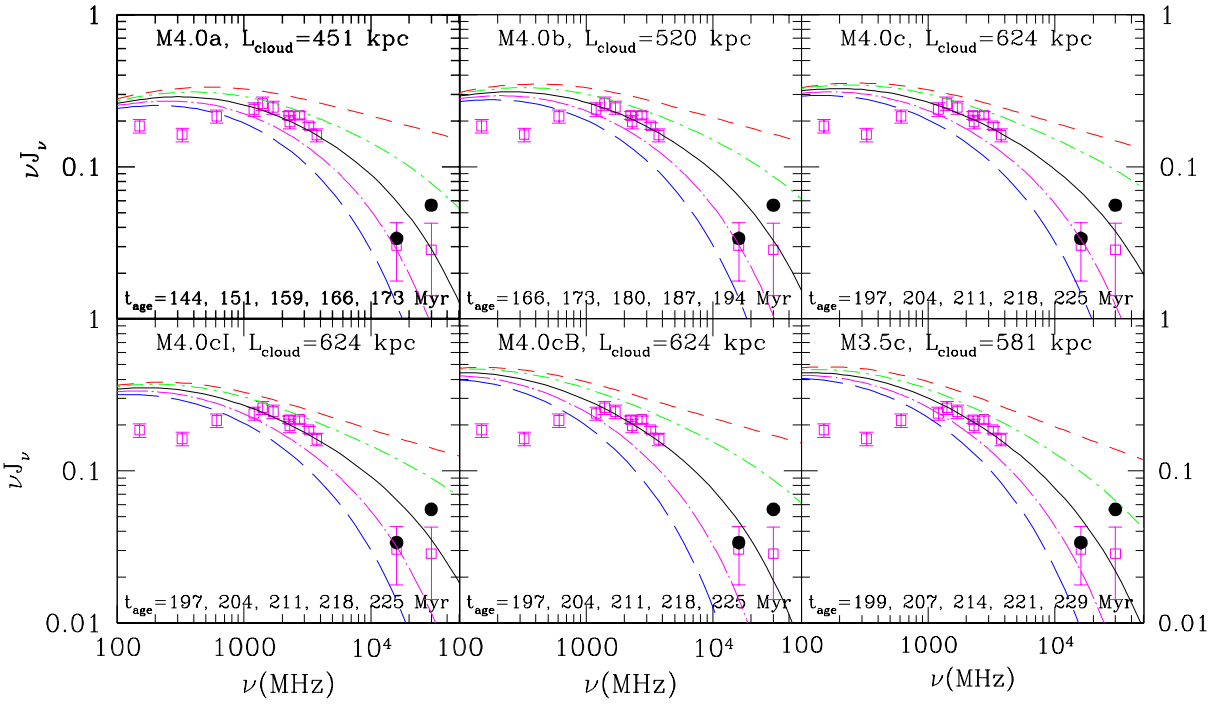

Figure 5. Time evolution of volume-integrated radio spectrum at five shock ages, specified in each panel, are shown in chronological order by the red dashed, green dot-dashed, black solid, magenta dot-long dashed, and blue long dashed lines. The open magenta squares and the error bars are the observational data of the Sausage relic taken from Stroe et al. (2016). The solid black circles at 16 GHz and 30 GHz are the data points, multiplied by factors of 1.11 and 1.96, respectively, which could represent the SZ-corrected fluxes (Basu et al. 2016).

gave much better visual impressions for the comparison between the predicted and the observed spectra.

4. SUMMARY

Many of observed features of giant radio relics are thought to be explained by the shock acceleration model: elongated shapes on scales of Mpc, radio spectral index steepening toward the cluster center, and high polarization levels (van Weeren et al. 2010; Stroe et al. 2016). Among some remaining puzzles concerning the shock acceleration model, in the case of the Sausage relic, we notice (1) the steep spectral curvature above GHz in the volume-integrated spectrum (Stroe et al. 2016) and (2) the discrepancy between the X-ray based shock Mach number, $M_{\rm X} \approx 2.7$ and the radio based value, $M_{\rm radio} \approx 4.6$ (Akamatsu et al. 2015; van Weeren et al. 2010). To understand these features, in earlier studies we explored the reacceleration scenario, in which a weak shock with $M_s \approx 3$ propagates through a finite-size cloud of the ICM gas, containing preexisting CRe with a flat spectrum (Kang & Ryu 2016; Kang 2016b). Considering the short cooling time of GeV electrons, however, it remains challenging to explain how to maintain such a flat population of high-energy electrons over a large preshock volume (Kang et al. 2017).

In this study, we explore an alternative model in which a shock of $M_s \approx 3-4$ sweeps through a preshock cloud containing low-energy fossil electrons and the electron aging is delayed by Fermi II acceleration by postshock turbulence. Here preexisting CRe with $\gamma_e \lesssim 300$ provide only seed electrons to Fermi I process, so the slope of the electron spectrum at the shock is determined by the sonic Mach number, i.e., $q = 4M_{\rm s}^2/(M_{\rm s}^2-1)$. This eliminates the unrealistic requirement of a flat power-law spectrum ($s = 4.1$) with a high energy cutoff ($\gamma_{\rm e,c} \approx 3-5\times10^4$) adopted in Kang (2016b) (Paper I). The observed width of the Sausage relic is too broad to be solely explained by electron cooling length (see the M4.0cN model in Figure 4). Hence, we assume that the postshock electrons are accelerated stochastically via transit time damping resonance off compressive MHD turbulence. We find that turbulent acceleration with $\tau_{\rm acc} \approx 10^8$ yr is required in order to match the observed broad profiles of the radio flux density, $S_\nu(R)$, of the Sausage relic. We note such a strength of turbulence acceleration is similar to what is required to reproduce the radio flux profiles of the Toothbrush radio relic (Kang et al. 2017).

Here we attempted to reproduce the observed profiles of $S_{153\rm MHz}$, $S_{608\rm MHz}$, and the spectral index α_{153}^{608} as well as the volume-integrated spectrum J_ν of the Sausage radio relic (Stroe et al. 2016). In the best fitting fiducial model, M4.0c (see Table 1 for the model parameters), the spherical shock with the initial Mach number $M_{s,i} = 4.0$ and the radius $r_{\rm s,i} = 0.8$ Mpc encounters the cloud of preexisting CRe and then sweeps out of the cloud after $t_{\rm exit} \approx 200$ Myr. It turns out that the degree of the spectral steepening above GHz in J_ν

strongly constrains the duration, $t_{\rm obs} - t_{\rm exit} \approx 10$ Myr, during which the shock propagates in the preshock region without fossil CRe. At the time of observation, the model shock weakens to $M_{\rm s,obs} \approx 3.2$ and the postshock temperature becomes $kT_{2,\rm obs} \approx 8.6$ keV, which are in reasonable agreements with X-ray observations (Akamatsu et al. 2015). Note that the M4.0c model does not reproduce the flattest observed index, $\alpha_{153}^{608} \approx 0.54$, at the relic edge, which requires a much stronger shock with $M_{\rm s} \approx 6.9$.

As shown in Figures 3 and 4, the spectral index profile, $\alpha_{153}^{608}(R)$, provides the most stringent constraints to the model parameters such as $M_{\rm s,i}$, $L_{\rm cloud}$, B_1, and $\tau_{\rm acc}$. The amount of fossil low-energy CRe that can produce the observed radio flux density corresponds to a pressure ratio $N = P_{\rm CRe}/P_{\rm g} \approx 10^{-4}$, which is dynamically insignificant. Considering that the observational error in J_ν is about 10%, we could argue that the model predictions in Figure 5 ($\log \nu J_\nu$ versus $\log \nu$) only marginally fit the observed integrated spectrum.

This study demonstrates that it is possible to explain most of the observed properties of the Sausage relic by shock reacceleration models with fossil relativistic electrons and an additional postshock Fermi II acceleration. This scenario is consistent with the observational fact that only a small fraction ($\sim 10\%$) of merging clusters host radio relics (Feretti et al. 2012). Thus we favor the DSA reacceleration model in which radio relics are generated preferentially when merger-driven shocks encounter the regions containing preexisting low-energy CRe.

ACKNOWLEDGMENTS

This research was supported by Basic Science Research Program through the National Research Foundation of Korea (NRF) funded by the Ministry of Education (2014R1A1A2057940) and NRF grant (2016R1A5A1013277). The author thanks A. Stroe and J. M. F. Donnert for providing the radio flux data for the Sausage relic reported in Stroe et al. (2016) and Donnert et al (2016).

REFERENCES

Akamatsu, H., van Weeren, R. J., Ogrean, G. A., et al. 2015, Suzaku X-Ray Study of the Double Radio Relic Galaxy Cluster CIZA J2242.8+5301, A&AP, 582, 87

Basu, K., Vazza, F., Erler, J., & Sommer, M. 2016, The Impact of SZ Effect on Cm-Wavelength (1-30 GHz) Observation of Galaxy Cluster Radio Relics, A&AP, 591, A142

Brunetti, G., & Jones, T. W. 2014, Cosmic Rays in Galaxy Clusters and Their Nonthermal Emission, Int. J. of Modern Physics D, 23, 30007

Brunetti, G., & Lazarian, A. 2007, Compressible Turbulence in Galaxy Clusters: Physics and Stochastic Particle Reacceleration MNRAS, 378, 245

Brunetti, G., & Lazarian, A. 2011, Particle Reacceleration by Compressible Turbulence in Galaxy Clusters: Effects of a Reduced Mean Free Path MNRAS, 412, 817

Clarke, T. E., Randall S. W., Sarazin, C. L., et al. 2013, Chandra View of the Ultra-Steep Spectrum Radio Source in A2443: Merger Shock-Induced Compression of Fossil Radio Plasma?, ApJ, 772, 84

de Gasperin, F., Ogrean, G. A., van Weeren, R. J., et al. 2015, Abell 1033: Birth of a Radio Phoenix, MNRAS, 448, 2197

Donnert, J. M. F., Stroe, A., Brunetti, G., et al. 2016, Magnetic Field Evolution in Giant Radio Relics Using the Example of CIZA J2242.8+5301, MNRAS, 462, 2014

Drury, L. O'C. 1983, An Introduction to the Theory of Diffusive Shock Acceleration of Energetic Particles in Tenuous Plasmas, Rept. Prog. Phys., 46, 973

Ensslin, T. A. 1999, Radio Ghosts, in Ringberg Workshop on Diffuse Thermal and Relativistic Plasma in Galaxy Clusters, ed. P. S. H. Böhringer, L. Feretti, MPE Report 271, 275

Feretti, L., Giovannini, G., Govoni, F., & Murgia, M. 2012, Clusters of Galaxies: Observational Properties of the Diffuse Radio Emission, A&A Rev, 20, 54

Fujita, Y., Takizawa, M., Yamazaki, R., Akamatsu, H., & Ohno, H. 2015, Turbulent Cosmic-Ray Reacceleration at Radio Relics and Halos in Clusters of Galaxies ApJ, 815,116

Hong, E. W., Kang, H., & Ryu, D. 2015, Radio and X-Ray Shocks in Clusters Of Galaxies, ApJ, 812, 49

Kang, H. 2011, Energy Spectrum of Nonthermal Electrons Accelerated at a Plane Shock, JKAS, 44, 49

Kang, H. 2015, Radio Emission from Weak Spherical Shocks in the Outskirts of Galaxy Clusters, JKAS, 48, 155

Kang, H. 2016a, Reacceleration Model for the 'Toothbrush' Radio Relic, JKAS, 49, 83

Kang, H. 2016b, Reacceleration Model for the 'Sausage' Radio Relic, JKAS, 49, 145 (Paper I)

Kang, H., & Ryu, D. 2016, Reacceleration Model for Radio Relics with Spectral Curvature, ApJ, 823, 13

Kang, H., Ryu, D., & Jones, T. W. 2012, Diffusive Shock Acceleration Simulations of Radio Relics, ApJ, 756, 97

Kang, H., Ryu, D., & Jones, T. W. 2017, Shock Acceleration Model for the Toothbrush Radio Relic, ApJ, 840, 42

Ogrean, G. A., Brüggen, M., van Weeren, R., et al. 2014, Challenges to Our Understanding of Radio Relics: X-Ray Observations of the Toothbrush Cluster, MNRAS, 440, 3416

Paul, S., Iapichino, L., Miniati, F., Bagchi, J., & Mannheim, K. 2011, Evolution of Shocks and Turbulence in Major Cluster Mergers, ApJ, 726, 17

Pierrard, V., & Lazar, M. 2010, Kappa Distributions: Theory and Applications in Space Plasmas, SoPh, 265, 153

Pinzke, A., Oh, S. P., & Pfrommer, C. 2013, Giant Radio Relics in Galaxy Clusters: Reacceleration of Fossil Relativistic Electrons?, MNRAS, 435, 1061

Ryu, D., & Vishniac, E. T. 1991, The Dynamic Instability of Adiabatic Blast Waves, ApJ, 368, 411

Sarazin C. L. 1999, The Energy Spectrum of Primary Cosmic-Ray Electrons in Clusters of Galaxies and Inverse Compton Emission, ApJ, 520, 529

Skilling, J. 1975, Cosmic Ray Streaming. I - Effect of Alfvén Waves on Particles, MNRAS, 172, 557

Slee, O. B., Roy, A. L., Murgia, M., Andernach, H., & Ehle, M. 2001, Four Extreme Relic Radio Sources in Clusters of Galaxies, AJ, 122, 1172

Stroe, A., van Weeren, R. J., Intema, H. T., Röttgering, H. J. A., Brüggen, M., & Hoeft, M. 2013, Discovery of Spectral Curvature in the Shock Downstream Region: CIZA J2242.8+5301, A&AP, 555, 110

Stroe, A., Rumsey, C., Harwood, J. J., van Weeren, R. J., Röttgering, H. J. A., et al. 2014b, The Highest Frequency Detection of a Radio Relic: 16 GHz AMI Observations of the 'Sausage' Cluster, MNRAS, 441, L41

Stroe, A., Shimwell, T. W., Rumsey, C., et al. 2016, The Widest Frequency Radio Relic Spectra: Observations from 150 MHz to 30 GHz, MNRAS, 455, 2402

van Weeren, R. J., Brunetti, G., Brüggen, M., et al. 2016, LOFAR, VLA, and CHANDRA Observations of the Toothbrush Galaxy Cluster, ApJ, 818, 204

van Weeren, R., Röttgering, H. J. A., Brüggen, M., & Hoeft, M. 2010, Particle Acceleration on Megaparsec Scales in a Merging Galaxy Cluster, Science, 330, 347

van Weeren, R., Brüggen, M., Röttgering, H. J. A., & Hoeft, M. 2011, Using Double Radio Relics to Constrain Galaxy Cluster Mergers: A Model of Double Radio Relics in CIZA J2242.8+5301, MNRAS, 418, 230

Yan, H., & Lazarian, A. 2002, Scattering of Cosmic Rays by Magnetohydrodynamic Interstellar Turbulence, PhRvL, 89, 281102